FAST COMPRESSIONAL ALFVEN WAVES IN A TOKAMAK

Hironori Takahashi

PFC/JA-80-7

March 1980

Fast Compressional Alfvén Waves in a Tokamak*

Hironori Takahashi

Plasma Fusion Center
Massachusetts Institute of Technology
Cambridge, Mass. 02139
U.S.A.

Enhancement of cyclotron damping is theoretically evaluated based upon the wave E-field polarization which is modified by the two-ion hybrid resonance. The degree of enhancement and its asymmetry about the plasma center is consistent with experimental observations. The enhancement factor is very large at low plasma densities at which most of the past damping strength measurements have been reported, but approaches unity at high densities. This implies the predominance of pure cyclotron damping in future reactor-like deuterium plasmas in spite of the presence of minority protons. A simple antenna and a pair of limiters are sufficient to couple rf power with an overall power deposition efficiency of about 75 %. There is no evidence that parasitic loading accounts for a significant amount of the power.

*This work was supported by the United States Department of Energy through Contract EY-76-C-023073.

1. Introduction

One promising method of additional heating for bringing a tokamak plasma to thermonuclear temperatures is irradiation of the plasma by electromagnetic fields in the ion cyclotron range of frequencies ("ICRF" heating)*. The impressed radio frequency (rf) field near the ion cyclotron frequency generates in the plasma fast compressional Alfvén waves whose energy is absorbed by the ions (and possibly by electrons) through various field-particle interactions. One possible mechanism for dissipating wave energy is ion cyclotron damping.

In one-ion species plasmas immersed in the inhomogeneous B-field of a tokamak, fundamental and harmonic cyclotron resonances occur at different major radius locations for a given wave frequency. Damping of the fast wave is governed by the small left-handed component (E_+) of the wave E-field in the resonance layer. In the fundamental resonance layer, where the wave frequency equals the fundamental cyclotron frequency of the constituent ions, ions experience acceleration proportional to the magnitude of the E_+. However, their coherent motion tends to shield the E_+-field nearly completely from the resonance layer. The fundamental cyclotron damping is consequently weak in one-ion species plasmas. In the second harmonic resonance layer ion acceleration is proportional to the ion Larmor radius (ρ_i) and

*A historical review of the subject can be found in ref. 1

to the perpendicular gradient of the E_+. The gradient can be approximated by $k_\perp |E_+|$ in one-ion species plasmas, and the wave damping strength is proportional to $1/2\, \rho_i (k_\perp |E_+|)^2$.

In recent tokamak experiments using deuterium as the working gas, small concentrations of protons were always found as impurities. Such a mixture represents a more complicated situation: the proton fundamental cyclotron and the deuteron second harmonic cyclotron resonances occur at the same location, and, furthermore, a new resonance between these ion species ("two-ion hybrid resonance") comes into existence. Because of the proximity of the cyclotron and hybrid resonance layers mutual influence of these resonances plays an important role in determining the dominant damping processes and division of the absorbed power among different species. In this mixture shielding of the E_+ from the proton fundamental resonance layer is incomplete and the protons keep accelerating in a familiar spiraling motion. This so-called minority species damping is proportional to the magnitude of the E_+-field, and can be much stronger than the second harmonic damping when the proton concentration is small (a few percent). However, the relative damping strengths depend strongly on the parallel phase speed.

The two-ion hybrid resonance surface lies very close to the cyclotron surface for low proton concentrations and has two principal effects on the waves: alteration of the wave E-field polarization in the ion cyclotron resonance layer and

introduction of mode conversion near the hybrid resonance layer. Mode conversion is important whenever cyclotron damping at the hybrid surface is weak. This situation arises either when the proton concentration is large and the hybrid resonance surface lies well outside the cyclotron resonance layer, or when the waves are nearly perpendicularly incident on the hybrid layer. Alteration of the polarization caused by the hybrid resonance is important when the proton concentration is a few percent. A significant increase in the magnitude and gradient of the E_+-field on the side of the ion cyclotron resonance layer closer to the hybrid surface results in strong enhancement of the deuteron second harmonic damping. The minority species damping is also significantly greater than in the absence of the hybrid resonance.

In their pioneering work Adam and Samain 2) calculated the second harmonic cyclotron damping strength in one-ion species plasmas and the fundamental cyclotron damping by the minority species in two-ion species plasmas. Stix 3), who analyzed temporal evolution of the ion velocity distribution under fast wave heating, obtained similar results for the damping strength. The roles played by mode conversion at the two-ion hybrid resonance were analyzed independently by Swanson 4) and Perkins 5). Enhancement of the cyclotron damping caused by the two-ion hybrid resonance through modification of the wave E-field polarization was first recognized by Takahashi 1,6). The present paper extends these earlier results to quantitative evaluation of

the enhancement of the cyclotron damping.

A series of ICRF heating experiments was conducted in the ATC tokamak 7), and was the first under the conditions in which the ion heating could be critically evaluated. The principal results of these experiments, showing substantial heating of the plasma core, have already been reported in a short letter 8). In the present paper those aspects of the experiments concerning wave generation, propagation and absorption are reported. These experimental results are interpreted in terms of the theory of enhanced cyclotron damping. These interpretations are in contrast to other experiments explained in terms of mode conversion damping at the two-ion hybrid resonance.

In this paper the phrase, "proton fundamental cyclotron", is abbreviated as PFC as in PFC resonance. The phrase, "deuteron second harmonic", is shortened as DSH as in DSH heating. The phrase, "two-ion hybrid", is represented by IHB as in IHB mode conversion.

2.1 Wave Coupling System and RF Instrumentation

A schematic of the wave coupling system used in the ATC tokamak is shown in Fig. 1. The overall electrical system and mechanical structure exterior to the tokamak vessel are similar to those used in the earlier experiments in the ST tokamak 9). The internal structure of the ATC coupler is different in two

important respects: the absence of an electrostatic shield; and, the presence of limiters to protect the antenna from direct contact with the dense plasma. The absence of a shield makes the ATC structure considerably simpler to fabricate and install.

The central element in the coupling structure is an antenna located on the outer side (larger major radius side) of the plasma torus. It subtends an arc-angle of 135 degrees in the poloidal plane about the plasma center, which is nominally located at a major radius of 0.9 m, and has an inside radius of 0.19 m. The antenna is made of a copper strip, 1 in. wide and 1/4 in. thick, and is encased in a ceramic sheath. The limiters lie in poloidal planes separated by 0.2 m along the meridian plane and are located symmetrically on either side of the antenna. The sides of the limiters facing the antenna are covered by ceramic plates. The inside radius of each limiter is 0.17 m and the ceramic plate is recessed by 1/8 in. The limiters are electrically grounded to the vessel and have slits cut in the radial direction to reduce the rf return current near the plasma edge that would tend to cancel the rf field created by the antenna current.

In order to achieve efficient coupling in the face of relatively small radiation resistance it is important to obtain a high antenna current. This is accomplished through a resonant impedance matching network which is adjusted to bring a current maximum (voltage minimum) of the standing wave pattern to the

antenna center and is tuned for a resonance. The impedance of this tuned circuit is matched to the line impedance by a pair of stub tuners. As plasma reactive effects vary, the network becomes detuned and the antenna current diminishes. However, these effects are small under the heating experiment conditions and the matching remains good. The measured root-mean-square (RMS) antenna current reaches 450 amperes but is typically 200-300 amp. The incident and reflected powers are measured by two 50 db directional couplers. The reflected power is no more than 10 % of the incident power. This means that the power coupling efficiency (net coupled power/incident power) of the ICRF antenna in ATC is better than 90 %. A net rf power of up to 200 kw is coupled into ATC by this system without encountering a limit set by electrical breakdown.

The rf current in the antenna is monitored by a one-turn magnetic loop which is half an inch in diameter and placed 3/4 in. behind the antenna slightly below the antenna midpoint (see Fig. 1). This current transducer has a sensitivity of about 0.1 volt/ampere measured across a 50 ohm termination. A voltage null probe is also located 1/2 in. behind the antenna slightly above the antenna midpoint. The probe, similar in construction to a spherical Langmuir probe (1/16 in. in diameter), is used primarily to locate the voltage minimum point, but also to estimate the plasma density behind the antenna. A crude interpretation of the ion saturation current from this probe leads to an estimate of plasma densities of less than $10^{17}/m^3$

behind the antenna.

There are arrays of probes that measure the toroidal component of the wave B-field. The relative phase of two probe signals is determined either by observing them directly on an oscilloscope or by means of an analog phase comparator constructed for this purpose. The phase measurements yield information on the poloidal mode number and toroidal wavelength of the fast wave.

One important measure of the antenna performance is its equivalent series loading resistance. It is defined as the ratio of the net rf power (RMS) fed into the antenna to the square of its rf current (RMS), and is determined by means of an analog device which will be referred to as the loading resistance (R_{sy}-) computer in this paper. The computer is useful in following rapid variation of the loading resistance caused by toroidal eigenmodes. The loading resistance is typically 1-2 ohms under plasma heating conditions compared to about 0.1 ohm in the absence of the plasma. Thus, only about 5-10 % of the coupled power is dissipated in the circuit.

2.2 Discharge Characteristics

ATC is a tokamak with toroidal compression capability 7). All ICRF heating is, however, applied to uncompressed deuterium plasmas with a major radius between 0.84 m and 0.9 m. The rf generator frequency is fixed at 25 MHz which corresponds to the

DSH cyclotron frequency at 1.64 T. All attempts to heat the plasma are performed at moderate-to-high densities ($n_{e0}>2x10^{19}/m^3$) and with the cyclotron resonance layer placed near the plasma center. In this paper we refer to these conditions as "plasma heating conditions". For wave measurement purposes both the field and density are varied over much wider ranges: $n_{e0}=0.5-4.2x10^{19}/m^3$ and $B_0=1.2-1.9$ T. The discharge typically lasts 40 ms with a 10 ms rf pulse usually applied 20-25 ms aftef discharge initiation.

The most important impurity for the considerations of wave absorption is hydrogen. An accurate measurement of its density is difficult, but the proton-to-deuteron ratio is estimated 10) to be at most 5 %. This upper bound is obtained from the fact that no recognizable peak exists in the wing of the D_β spectral line at a location where the H_β line is expected. Small proton-to-deuteron ratios found in ATC are in contrast to those (~20 %) in TFR experiments 11), and are among the reasons for interpreting the observed wave damping strength in terms of enhanced cyclotron damping rather than mode conversion. Throughout this paper the proton concentration (proton-to-electron ratio) is taken to be small (<5 %) and is arbitrarily assumed to be 3 %, whenever a numerical value is needed. More detailed descriptions of the experimental facilities and environment can be found in a laboratory report 12).

3.1 Fast Wave Propagation in ATC

In ATC plasma the wave damping length is large compared to the (minor) radial extent of the plasma. This makes the wave propagation and damping amenable to separate analyses: propagation characteristics and field structure of undamped waves are first obtained and the damping strengths are then calculated based upon the known field structure. We first consider the fast waves in a straight cylindrical waveguide partially filled with a cold uniform plasma and immersed in a uniform longitudinal magnetic field. Eigenmode solutions for such a system were obtained by Bernstein and Trehan 13) for general non-axisymmetric modes. A theory of excitation of azimuthally symmetric eigenmodes was developed by Stix 14). The theory 15) used here is an extention of the latter to more general non-axisymmetric cases using the eigen-solutions of the former. Wave energy density, Poynting flux, group velocity, and radiation resistance are also calculated. (The term, "radiation resistance", is used for the antenna loading resistance in the absence of toroidal effects.) In particular, the group velocity averaged over the waveguide cross-section is computed as the ratio of the time-averaged Poynting flux integrated over the waveguide cross-section to the wave energy per unit length of the waveguide. Both the Poynting flux and wave energy consist of contributions from the plasma and vacuum regions within the waveguide, and the computed group velocity depends upon the size of the vacuum region.

The ATC vacuum vessel is oblong in cross-section (see Fig. 1), encloses a large vacuum space on the small major radius side and is difficult to model accurately in theoretical calculations. On one hand, theoretically calculated group velocity tends to be too small because of the failure to account for the large vacuum space. Calculations of the loading resistance, on the other hand, depend critically on the relative sizes of the plasma, antenna and vacuum vessel. The vacuum vessel is represented by a torus of circular cross-section with a minor radius of 0.21m. Were the theoretical vessel to enclose the same volume as the actual vessel, its equivalent radius would be 0.27m. Eighty percent of the actual vessel walls are made of bellows structure, but the theoretical model assumes smooth stainless-steel walls. The inhomogeneous plasma is represented in theory by a plasma of constant density equal to the volume average of the actual density. Ion and electron temperature variations with time are taken from a typical discharge at each density level.

A discrete fast wave eigenmode * in a plasma filled waveguide can be identified by a set of radial(l) and azimuthal(m) mode numbers. It is convenient to speak in terms of the perpendicular ($N_\perp = k_\perp V_A/\omega$) and parallel ($N_\parallel = k_\parallel V_A/\omega$) Alfvén refractive indices 3), where $k_\perp$, $k_\parallel$, V_A and ω are, respectively, the perpendicular and parallel wave numbers, Alfvén speed, and wave angular frequency. At sufficiently low densities the fast waves

*See, e.g., Fig. 2 of ref. 3 or Fig. 6 of ref. 12.

in a completely filled waveguide suffer a cut-off ($N_{\parallel}^2<0$) and are unable to propagate along the waveguide. In a partially filled waveguide the cut-off exists for the m=0 and all negative-m azimuthal modes (for the field variation of the form exp $i(k_{\parallel} z+m\theta-\omega t)$). However, the lowest radial modes of all positive-m modes propagate at very low densities *. (They can presumably propagate at all densities.) As the density increases, a cut-off mode may become propagating, at which point $N_{\perp}^2=1$ and $N_{\parallel}^2=0$. We term this condition the "onset" of a new propagating mode. As the density increases further, the parallel wavelength becomes progressively shorter. Because of the different dependence of the PFC, DSH and IHB damping strengths on the parallel wavelength, the mode goes through different phases in each of which a different mechanism is responsible for the wave damping. The exact plasma conditions under which the onset of a mode takes place is sensitively dependent on the radial density profile 17) and the presence of the vacuum space. Because of the approximate nature of the representation of the actual ATC vacuum vessel and the uniform plasma model used in the present theory, the model's prediction of the onset conditions is not expected to be accurate.

Toroidal effects on wave propagation are accounted for by superposing the fields of the waves circumnavigating around the

*This was demonstrated by numerical examples by Paoloni 16) for m=0 and +1 modes. Similar calculations indicate that the same is true for all positive-m modes.

torus. The resultant fields depend upon both the phase shift and damping that the waves suffer as they go around the torus. Under such conditions processes of wave generation, propagation, and damping are closely intertwined and isolated investigation of each process is difficult in practice. Nevertheless, studies of the loading resistance and wave amplitude under different plasma conditions provide evidence for wave generation and clues for the physical mechanisms of wave damping.

Suppose that the antenna carrying unit rf current generates a wave field of amplitude, s, in the absence of the toroidal effect. In a toroidal geometry with dissipation, the waves experience a complex phase shift $i\tilde{k}_{\parallel}L$ each time they go around the torus, where $\tilde{k}_{\parallel}$ is the complex parallel wave number and L the toroidal circumference. The total field for an rf current of I for the waves propagating around the torus many times is obtained by summing an infinite series,

$$\begin{aligned} S &= sI(1 + \exp i\tilde{k}_{\parallel}L + \exp 2i\tilde{k}_{\parallel}L + \ldots) \\ &= sI/(1 - \exp i\tilde{k}_{\parallel}L) \end{aligned} \qquad (1)$$

When the plasma conditions are appropriate for a constructive interference of the wave fields, the cavity becomes resonant. As the conditions (principally the density) vary with time, a series of such toroidal cavity resonances should be observed. At a resonance and at an anti-resonance (n is a half-integer) S is pure real and is given respectively by,

$$S_R = sI_R/(1 - \alpha) \quad (2)$$

$$S_A = sI_A/(1 + \alpha) \quad (3)$$

where $\alpha = \exp(-k_i L)$ and k_i is the imaginary part of the parallel wave number. I_R and I_A are the rf currents at the resonance and anti-resonance, respectively. These two quantities are experimentally measureable. It should be noted that the toroidal resonance can be a travelling (as opposed to a more usual standing) wave resonance: the waves travelling in only one direction can cause a resonance. This has some practical consequences 1). Its wavelength can be determined simply by measuring the relative phases of the wave field at two or more points around the torus. The travelling waves also deposit energy more uniformly around the torus than the standing waves. If the so-called mode splitting, caused by unequal influence of the poloidal B-field on the left- and right-running waves, is indeed present, all experimentally observed resonances, other than the m=0 modes with no mode splitting, must be the travelling wave resonances. (No experimental demonstration of this fact has been reported in the literature.)

The oscillogram in Fig. 2 shows time variation of the wave amplitude (rf envelope) measured by the probes located at 90 degrees around the torus away from the antenna nearly directly above(T) and below(B) the plasma axis. The different amplitudes

of the two signals are caused by a slightly off-centered plasma. The peaks and troughs of the wave amplitude evidently correspond to the occurence of toroidal resonances and anti-resonances. The theoretical calculations of the wave amplitudes corresponding to the experimentally observed density variations confirm the presence of the peaks and troughs. However, one-to-one correspondence of these peaks cannot be established in the ATC experiments, becuase of the approximate nature of the theoretical model. It was shown in the earlier experiments 9) in the ST tokamak, however, that the density and B-field dependences of the loading resistance peaks closely followed the fast wave dispersion relation. For these experiments the circular waveguide model was a better representation of the actual vacuum vessel and the theoretical calculations accounted for the density inhomogeneity.

3.2 Wave Damping Measurements

A set of R_S-computer signals is shown in Fig. 3. The toroidal B-field is different for each of the oscillograms. (The plasma conditions are also slightly different.) In each case the density increases monotonically by a factor of two or less over the pulse period, except in the left-most oscillogram for which the density reaches a maximum during the pulse. The locations of the DSH (deuteron second harmonic) cyclotron resonance surface are indicated in the figure. The data are taken at density levels sufficiently low (n_{e0}=7.5-9.6x10^{18}/m^3 at the mid-point of

the pulse) that the m=0 and all negative-m modes are cut-off. The prominent peaks in these oscillograms are determined to be the m=+1 mode by phase measurements of magnetic probe signals. (However, small-amplitude, higher azimuthal modes (m>+1) may also be present simultaneously in the signals.) Toroidal wavelength measurements of selected resonant peaks indicate toroidal mode numbers of 2-4. When the cyclotron resonance surface is within the plasma, the toroidal resonance is broader, indicating the presence of damping processes on or near the resonance surface.

Quantitative evaluation of the damping strength can be made from the magnetic probe signals such as those shown in Fig. 2. The quantity, s, in eqs. (2) and (3), which is proportional to the radiation resistance, is in general, not directly measurable. However, this can be eliminated by taking the ratio of the wave amplitude at a resonance to that at an adjacent anti-resonance, if the variation of the radiation resistance for a small change in plasma parameters is neglected. The ratio is related to the wave damping length(L_D) through *,

$$L_D/L = [\ln(\gamma+1)/(\gamma-1)]^{-1} \qquad (4)$$

where $\gamma = I_A S_R / I_R S_A$. The normalized damping length (L_D/L) is the number of times the waves go around the torus before their amplitudes e-fold. The wave damping length is related to the

*Typographical errors in eq. 9 of ref. 1 are corrected here.

resonant cavity quality factor (Q) through,

$$L_D \equiv 1/k_i = 2Qu_g/\omega \qquad (5)$$

where u_g is the parallel group velocity. It should be noted that the group velocity varies widely depending upon the mode and that a large Q mode does not necessarily imply a large L_D mode. In experiments either the damping length or the Q-factor is directly determined and the other is derived through eq. (5). Some ambiguities would be introduced through this conversion unless the group velocity is accurately known.

The damping length determined using eq. (4) is shown 18) in Fig. 4(a) for the conditions corresponding to the oscillograms shown in Fig. 3. The abscissa is the major radius location of the DSH (or PFC) resonance surface. The observed modes are the m=+1 azimuthal modes, but may include different toroidal mode numbers in the range of 2-4. When the resonant surface is outside the plasma on the high field side ($R(\Omega=2)=70$ cm), the damping is weak and the waves go around the torus some 13 times before their amplitudes e-fold. This damping is interpreted as the damping caused by the wall resistance. The measured damping length is one-twentieth the theoretical wall resistive damping length computed for these modes in circular cylindrical waveguide made of perfectly smooth stainless-steel walls. The observed damping length appears reasonable, however, because of the increased path lengths of the wall currents due to (1)the

elongated vacuum vessel cross-section (a 1.6-fold increase in poloidal circumference), (2)the partial bellows structure (an average of five-fold increase in toroidal circumference), (3)the presence of ports and other obstructions to the wall current paths and (4)the surface roughness (0.8-13.0 μm) * comparable to the skin depth (8.5 μm), all of which tend to increase wave damping strength. In the following calculations the wall damping length is taken to be one-twentieth the value for the perfect cylindrical surface. When the resonant layer is within the plasma, the normalized damping length is reduced to about 2. The ratio, 13/2=6.5, of the damping lengths with and without the resonance is a measure of the effectiveness of energy deposition by the fast wave: about 90% (6.5/(1+6.5)=0.87) of the power is deposited within the plasma and about 10% in the walls. These observations lead to an optimistic view for fast wave heating of tokamak pasmas.

When the resonant layer is outside the plasma on the low field side ($R(\Omega=2)=110$ cm), the damping is stronger than on the high field side indicating the presence of some additional damping mechanisms. The nature of these damping mechanisms is not well understood. There are, however, indications observed on the charge exchange (CX) analyzer signals that suggest possible non-linear processes taking place on or near the cyclotron surface in the tenuous plasma outside the nominal plasma radius.

*The range of roughness of commercially available cold rolled stainless-steel sheets.

In Fig. 5 oscillograms of the charge exchange neutral analyzer and R_S-computer signals are shown together with a schematic showing the relative locations of the plasma, antenna and cyclotron resoanace layer. Very large-amplitude, sharp spikes are observed on the high-energy channels of the CX analyzer nearly exactly coincident with the appearance of a toroidal resonance peak in the loading resistance. The CX signals rise and fall very rapidly with a time scale comparable to the time constant (300 μsec) of the analyzer, indicating that the energetic ions are contained only for a very short time. This suggests that the observed phenomenum is taking place in the plasma periphery. When the resonance layer is deep inside the main body of the plasma, or, outside the plasma on the high field side, no such spikes are observed. One possible explanation for the absence of spikes under these conditions can be either that the energetic ions are not contained long enough to reach the analyzer unless they are created right in front of it, or that the neutrals created upon charge exchange of the energetic ions can not penetrate through the dense main body plasma to reach the analyzer without being reionized. However, the difference of the wave damping strengths when the resonance is on the opposite sides of the plasma suggests that the observed phenomenum takes place mostly on the low field side. Furthermore, the coincidence of the spikes with the occurence of a toroidal resonance, at which the wave electric field becomes large, is indicative of a threshold nature of the phenomenum.

A notable feature of the damping curve in Fig. 4(a) is that the region of the maximum damping is not symmetric with respect to the plasma axis at R_0=87 cm and is shifted toward the larger major radius side 19). This shift was also observed in TFR experiments 20). Another manifestation of the asymmetry 21) is shown in Fig. 4(b). The abscissa is identical to that of Fig. 4(a). The ordinate is the output voltage of a bolometer facing the plasma and is proportional to the power loss due to charge exchange and radiation integrated over the period of rf pulse. The net difference between discharges with and without the heating pulse is plotted. A broad peak is located on the larger major radius side of the plasma axis where the center of the strong damping region is also located. Under these conditions the rf power is evidently more efficiently absorbed by the ions, some of which become lost through charge exchange and intercepted by the bolometer.

Another set of output signals * from the R_{ω}-computer is shown in Fig. 6. The resonant surface ($R(\Omega=2)$=88 cm) is located in the vicinity of the plasma center (R_0=87-89 cm) for all cases except the lowest density case (No. 1). The electron density levels are different for each case and are shown in the figure. The lowest density case (No. 1) is taken under conditions nominally identical to those of the center oscillogram of Fig. 3. Toroidal resonance peaks of the loading resistance become progressively

*The incorrect label of the ordinate of Fig. 4 and numbering of oscillograms in Fig. 5 of ref. 1 are corrected here.

broader at higher densities and are difficult to recognize at the highest density level. The latter is a typical condition under which most heating experiments are undertaken. In the absence of isolated resonant peaks in these high density cases the experimental determination of the damping strength based upon eq. (4) is not possible.

3.3 Cyclotron Damping

We first compare the experimentally observed time variations of the loading resistance and wave damping strength with predictions based upon the theory of cyclotron damping. One low density case, for which direct experimental measurements of the damping strength are made, and one high density case, for which the measurements are not available, are examined in some detail. The electron Landau damping and transit time magnetic pumping (TTMP) are also included in the calculations, but their effects on the fast waves are weak under the ATC conditions. The damping strengths needed in eqs. (1)-(3) are derived from Stix's results 3) given in terms of the quality factor of a resonant cavity. They are for the minority (Q_I), second harmonic (Q_{II}), and Landau/TTMP (Q_e) damping given respectively by,

$$Q_I = 2\left(\frac{a}{R_0}\right)\left(\frac{n_D}{n_H}\right)\left[1 + \frac{9\pi}{16}\left(\frac{n_H}{n_D}\,\frac{u_{\parallel}}{v_H}\right)^2\right] \qquad (6)$$

$$Q_{II} = \frac{2\left(\frac{a}{R_0}\right)}{(k_\perp \rho_D)^2\left[1-\left(\frac{r_{res}}{a}\right)^2\right]^{1/2}} \tag{7}$$

$$Q_e = \frac{2}{\pi^{1/2}\beta_e\left(\frac{u_\parallel}{v_e}\right)\exp-\left(\frac{u_\parallel}{v_e}\right)^2} \tag{8}$$

Here, a and r_{res} are respectively the plasma minor radius and the distance between the cyclotron resonance layer and the plasma axis. n_D and n_H are, respectively, the deuteron and proton densities. $u_\parallel$, v_H and v_D are, respectively, the wave parallel phase speed, proton, and deuteron thermal speed. β_e is the ratio of the electron thermal pressure to the magnetic pressure.

In deriving these results Stix accounted for the reduction of the E_+-field at the cyclotron surface due to the presence of resonant minority protons. However, the E_+ and its gradient were evaluated at the resonance surface and were taken to be constant across the thin resonance layer. These were reasonable approximations for one-ion species plasmas, but neither enhancement of the cyclotron damping nor the mode conversion, both caused by the presence of the two-ion hybrid resonance, was included. Further approximations introduced in Stix's analysis were the assumptions that the E_+ was also constant along the resonant surface and that $N_\perp^2 \simeq 1$. The latter would result in an over-estimate of the second harmonic damping strength by a factor up to four for those modes that are not near their onset.

It is often stated that minority damping is much stronger than second harmonic damping when the minority concentration is a few percent. However, the strong wavelength dependence of Q_I in eq. (6) should be noted. As the wavelength of a new propagating mode becomes progressively shorter with rising plasma density, the dominant damping mechanism rapidly changes from the second harmonic to the minority damping. Higher radial modes with a large $k_\perp$ and small $k_\parallel$ are more strongly damped by the second harmonic damping. Near the onset, both damping strengths are proportional to the ion temperature. Away from the onset and at sufficiently high temperatures, Q_I becomes independent of temperature, which may have interesting consequences because the second harmonic damping becomes dominant for all wavelengths in high temperature reactor-like plasmas. Note the symmetry of the second harmonic damping with respect to the relative locations of the resonant layer and plasma axis (eq. (7)). This is in contrast to the experimental observations discussed earlier (Fig. 4(a)).

Theoretical loading resistance variation for the low density case is shown in Fig. 7(a) and should be compared with the oscillogram at the center of Fig. 3. Toroidal resonances are designated by sets of radial(l), poloidal(m) and toroidal(n) mode numbers. The radiation resistance is first computed based upon the theoretical model outlined in Sec. 3.1 and the toroidal effect is intrduced through eq. (1). The imaginary part of the parallel wave number needed in this equation is obtained from

Q-factors given in eqs. (6)-(8) by converting them to the damping length through eq. (5). By using time-varying density, the effects on the loading resistance of each mode going through different phases of its "life span" can be simulated. There are only two poloidal modes (m=+1 and +2) that carry appreciable power. The loading resistances of the individual modes up to m=+3 as well as the total resistance are shown in Fig. 7(a). The damping lengths predicted from theory are too large, so that the theoretical toroidal resonant peaks which can reach 6.3 ohms are much larger than the largest experimental values of 0.5 ohms. Note the ambiguities introduced by converting the Q-factors to the damping length: the discrepancies caused by too large Q-factors predicted by the theory are partly offset by a too small group velocity used in the conversion. Without this offsetting effect the difference between experiment and theory would be bigger.

The theoretical values of the minority(I), second harmonic(II), electron Landau/TTMP(E), wall resistive(W), and total(T) damping lengths are tabulated in Table I for each toroidal mode shown in Fig. 7(a). The damping lengths predicted by this theory are comparable for the PFC and DSH damping for these toroidal modes, and are much greater than the wall resistive damping length. If these predictions were true, then most of the power would be dissipated in the walls and there would be no significant change in the measured damping length as the resonant layer moved into the plasma. The previous section shows that this is not the case:

the measured damping length is smaller than the tabulated values by factors between 18 and 120, depending upon the modes. No entries are made for the electron Landau/TTMP damping in the table because it is completely negligible ($L_D/L>10^4$) for these cases.

Fig. 8(a) shows the computed loading resistance variation for the high density case which should be compared with the top right oscillogram (No. 5) of Fig. 6. There are five propagating modes that carry appreciable power (the first radial modes of m=-1 through m=+2 and the second radial mode of m=+1). The loading resistance of each mode and the sum over all modes are shown in the figure. (The m=+1 curve is the sum of its first and second radial modes.) The theoretical radiation resistance of a mode is in general highest at its onset, and is further enhanced by the fact that the long wavelength n=1 toroidal mode comes into resonance immediately following the onset. The first radial mode of m=-1 poloidal mode and the second radial mode of m=+1 mode have the onset at nearly identical times (at about 23 ms). The n=1 toroidal modes of these poloidal modes create a high peak of the loading resistance. Such abrupt changes in the loading resistance are not observed in the experiments, and are considered to be due to the deficiency of the uniform plasma model. The other resonant peaks in Fig. 8(a) are more prominent than the experimentally observed ones, indicating actual damping strengths stronger than the theoretical predictions. However, the differences are not as pronounced as in the low density case

(Fig. 7(a)).

Theoretical values of the minority(I), second harmonic(II), electron Landau/TTMP(E), wall resistive(W), and total(T) damping strengths are tabulated in Table II for each toroidal mode shown in Fig. 8(a). The DSH damping is the strongest mechanism for all low toroidal number modes ($n \leq 3$). The m=-1 poloidal modes and the l=2 radial modes appear only at high densities and are much more strongly absorbed by the DSH damping than the PFC damping. These modes would deposit most of their energy directly into deuterons and make fast wave heating less susceptible to "thermal runaway" of the minority species 22). Unlike the low density case, the theoretically predicted total damping is now dominated by power dissipation in the plasma rather than in the walls. The theoretical power deposition efficiency ranges from 74 % to 97 % for these modes. The efficiency is generally better for those modes that carry large shares of the total power. Although no direct measurements are available, comparisons of the theoretical loading curve with the experimental one indicate that the computed damping strengths are still an underestimate of the actual values. The actual efficiency is therefore expected to be greater than these figures. Electron Landau/TTMP damping is completely negligible ($L_D/L > 10^4$) except where entries are made in the table.

The theory in this section is based upon a uniform plasma model with the cyclotron and Landau/TTMP damping strengths obtained by

Stix. The uniform plasma model is inaccurate in predicting the mode onset, and one-to-one correspondence of the toroidal resonant peaks cannot be obtained. This discussion has shown that the predicted damping lengths at low densities (n_{e0}=0.5-1.0x$10^{19}/m^3$), where the experimental measurements for individual modes can be made, are too large by a large factor (18-120). The dependence of the damping length on the resonant layer location also fails to predict the observed asymmetry about the plasma center. Although the damping strength of individual modes cannot be measured at higher densities, where many overlapping modes are present, the predicted time variation of the loading resistance indicates that the discrepancies are much smaller.

3.4 Enhanced Cyclotron Damping

We next consider whether better agreement can be found between theory and experiments if enhancement of the cyclotron damping caused by the presence of the two-ion hybrid resonance is included. For small proton concentrations ($C_H \sim 3$ %) the proton-deuteron hybrid resonance surface lies only a small distance ($\sim$ 1 cm) away from the cyclotron resonance surface. * The cyclotron and hybrid resonance layers overlap with each other and their mutual influence must be taken into account. The fast

*The geometry of the two-ion hybrid resonance surface, cyclotron resonance surface and fast wave cut-off surface can be found, e.g., in Fig. 6 of ref. 1 and in ref. 5.

wave has only a small left-hand polarized electric field component in one-ion species plasmas. However, the hybrid resonance (an electrostatic resonance) tends to produce a linear E-field polarization (i.e., $E_+=E_-$) and thus to enhance the magnitude of E_+-field. The proton cyclotron resonance (an electromagnetic resonance) tends to make the polarization both circular and right-handed and thus to reduce the magnitude of E_+-field. (The theories by Adam and Samain 2) and by Stix 3) include only the latter effect.) Within the region between the two resonance surfaces both the magnitude and gradient of the E_+-field are greater than in the absence of the hybrid resonance. The magnetic field inhomogeneity across the plasma cross-section must be included into the analysis, and a treatment in cylindrical geometry becomes difficult. However, because of the relatively thin and straight geometry of the cyclotron and hybrid resonance layers in the important central plasma region, the situation may be amenable to an approximate treatment in a simpler slab geometry.

Boundary value problems in slab geometry with an inhomogeneous B-field and a non-uniform warm plasma were solved numerically by Takahashi 1) to obtain the E-field structure. The theory was based upon a second-order differential equation (eq. (23) of ref. 1) that treated the PFC damping in a self-consistent manner, but the DSH damping was not included. Thus, the theory was strictly valid only when the latter had small effects. Because of the proximity of the cyclotron resonance layer, the hybrid

resonance is heavily damped: the real and imaginary parts of the perpendicular wave number computed for the local plasma properties were comparable and the real part of the coefficient of the second order derivative term in the differential equation did not vanish at the hybrid layer. A criterion for such weak resonances was obtained earlier 1). The resonance is weak when the following inequality is satisfied:

$$C_H \equiv \frac{n_H}{n_e} \leq \frac{2}{1.082} C_D \left(n_\parallel \frac{v_H}{c}\right) \left[\frac{1}{1-\Omega_D^2} + \frac{n_\parallel^2}{\Omega_{PD}^2}\right] \qquad (9)$$

Here, $C_D = n_D/n_e$, $\Omega_D = \omega_{cD}/\omega$, $\Omega_{PD} = \omega_{PD}/\omega$, and ω_{cD}, ω_{PD} and c are, respectively, the deuteron cyclotron and plasma frequencies and the speed of light in vacuum. In the present paper we are also concerned with such weak resonance cases.

In Fig. 9 the E-field structures for specific cases are reproduced from ref. 1. The x-coordinate is in the direction of inhomogeneity with its origin at the slab center. The abscissa of the figure is $R_0 - x$, where $R_0 = 0.9$ m is the scale length of the B-field inhomogeneity ("major radius") at the center. The tokamak axis is to the right of the figure. The slab half-width ("minor radius") is, a=0.17 m, and $n_{e0} = 2.5 \times 10^{19}/m^3$. The top figures are variations of the E_x-field across the slab for three different

values of magnetic field: one for which the PFC resonance is located at the center and two others for which the resonance is displaced by 0.06m on either side of the center. The lower figures are variations of the E_+-field for the corresponding three cases. (Note the ten-to-one difference in the ordinate between the two groups of figures.) Locations of the ion cyclotron (ICR) and two-ion hybrid (HBR) resonance surfaces are indicated in these figures.

Effects of the weak hybrid resonance appear as small bumps on the E_x-curves (The E_y is little affected) in Fig. 9. The effects are stronger on the low field side of the axis, evidently as a result of the fact that the field and density gradients are in the same direction there. However, influence of the hybrid resonance on the E_+ is significant. Compare the C_H=0 and 3 % cases shown in the lower central figure. The large difference is a consequence of the fact that the field polarization is strongly altered by the IHB and PFC resonances. Particularly noteworthy here is the appearance of a very steep gradient of the E_+ over a narrow region between the cyclotron and hybrid resonances. In the case shown in the lower left figure the gradient in this region is enhanced by one order of magnitude over the value obtained in the absence of the hybrid resonance. It is then expected that the DSH damping should be enhanced by two orders of magnitude. Since the magnitude of the E_+ can also be greater than without the hybrid resonance, the PFC damping could also be enhanced. Furthermore, the dependence of both of

these damping strengths on the resonance layer location is asymmetric with respect to the plasma center. A more quantitative analysis is presented in the remainder of this section.

Ions that move across the cyclotron resonance layer receive a kick in their perpendicular energies due to the cyclotron acceleration. The power absorbed by the ions can be calculated by taking a statistical average of these incremental energy gains. For a slab of unit height and depth the power absorbed by the protons and deuterons is given respectively by 6),

$$P_I = 4\pi R_c \left(\frac{\omega_{PH}^2}{\omega}\right)\frac{\varepsilon_0}{4}|E_+(x)|^2_{x=x_c} J_I \tag{10}$$

$$P_{II} = 4\pi R_c \left(\frac{\omega_{PD}^2}{\omega}\right)\frac{\varepsilon_0}{4}|E_+(x)|^2_{x=x_c} \left(\frac{\rho_D}{2a}\right)^2 J_{II} \tag{11}$$

Here, x_c and R_c are the x-coordinate and the "major radius" of the cyclotron resonance surface. ω_{PH} and ρ_D are, respectively, the proton plasma frequency and the deuteron Larmor radius. The integrals, J_I and J_{II}, are given by,

$$J_I = \frac{2}{\pi^{1/2}} \int_0^\infty d\zeta_H |\mathcal{E}(\zeta_H)|^2 \exp - \zeta_H^2 \tag{12}$$

$$J_{II} = \frac{2}{\pi^{1/2}} \int_0^\infty d\zeta_D |\mathcal{F}(\zeta_D)|^2 \exp - \zeta_D^2 \qquad (13)$$

where

$$\zeta_M = (u_{\parallel}/v_M)(x - x_c)/R_c \qquad (14)$$

$$\mathcal{E}(x) = E_+(x)/E_+(x_c) \qquad (15)$$

$$\mathcal{F}(x) = a[dE_+(x)/dx]/E_+(x_c) \qquad (16)$$

Dimensionless quantities, $\mathcal{E}(x)$ and $\mathcal{F}(x)$, are the E_+-field and its gradient normalized by the E_+ at the resonance surface. The subscript, M, in eq. (14) refers to either proton(H) or deuteron(D) and v_M is the most probable speed of the M-species ions. In this analysis the wave number, k_y, (y axis perpendicular to the x-coordinate and B-field) is assumed to be zero.

If the E_+ is evaluated at the resonance surface and assumed constant across the resonance layer, then $\mathcal{E}(x)=1$ and J_I integrates to unity. Thus, the approximation used by Stix would correspond to $J_I=1$ and the actual value of J_I represents the "enhancement factor" of the PFC power absorption. Similarly, if the E_+ gradient is approximated by $k_\perp|E_+|$ and evaluated at the resonance surface, J_{II} equals to $(k_\perp a)^2$. Stix further assumed $N_\perp^2=1$, or equivalently, $k_\perp=k_A$, where k_A is the Alfvén wave number (ω/V_A). $J_{II}/(k_A a)^2$ is therefore the enhancement factor for the

DSH power absorption. The results of the calculations for some specific cases are presented in the remainder of this section. For these calculations the integrals in eqs. (12) and (13) are evaluated numerically using the field variation obtained from the solutions of the boundary value problem discussed in an earlier paragraph. The parameters common for all cases are: a=0.17 m, R_0=0.9 m, C_H=3 %, and the on-axis ion tempeature, T_{i0}=200 eV.

Several computed quantities for four different locations of the cyclotron surface are presented in Table III. P_I and P_{II} are, respectively, the power absorbed by the PFC and DSH damping within a slab of unit height and depth. These values are for the waves travelling in one direction only, and are normalized in such a way that the Poynting flux is 1 MW per unit height of the slab. Power absorption by both mechanisms is strong when the resonance surface is located in the low field side of the center, which is consistent with the observed asymmetry in the wave damping (Fig. 4(a)). The asymmetry is particularly pronounced for DSH damping. If the deuterons absorb much more power when the resonance surface is in the low field side, power loss from the plasma through deuteron charge exchange should also be much greater under these conditions. This expectation is not inconsistent with the observed asymmetry of the bolometer signals discussed earlier (Fig. 4(b)). The eigenvalue for the parallel refractive index ($n_{||}$) is about 30 for all cases and thus would correspond to the toroidal mode number of 15. This is considerably greater than the toroidal mode numbers shown in

Figs. 6 and 7. (The slab geometry leads to the parallel wavelength considerably shorter than the cylindrical geometry with the same peak density. This is partly due to the fact that k_y is taken to be zero.) In these computed cases the PFC damping is about one order of magnitude stronger than the DSH damping, and thus the assumption underlying the theory is valid. When the resonance surface is located at the plasma center, the enhancement factors are respectively 1.8 and 5.2 for the PFC and DSH damping, but if the resonance surface is located at 0.04 m away from the plasma center on the low field side, the enhancement factors are respectively 2.8 and 13 *.

In Fig. 8(b) variation of the loading resistance is shown for the same case as (a), but with the PFC and DSH damping strengths multiplied respectively by 1.8 and 5.2. Since the enhancement factors should be different for different modes, the results given here are only approximations. However, they indicate that the modest enhancement factors expected from the theory of the two-ion hybrid resonance are sufficient to suppress the prominent toroidal resonance peaks and to make the appearance of the loading curve reasonably similar to experimental observations. The abrupt rise of the loading resistance at the onset of the two

*When the resonance surface is further away from the center and comes too close to the fast wave cut-off surface, these enhancement factors become very large, but the normalizing factor (the E_+ at the resonance surface) tends to zero. The enhancement factors lose their significance in these cases, since Stix's results were obtained based upon the plasma properties of the central core.

new modes and subsequent gradual fall-off (instead of gradual rise seen in Fig. 6) of the resistance are the principal discrepancies that are still evident.

Each mode with a given set of radial and poloidal mode numbers has a given radial variation of the E_+-field, and hence the radial power deposition pattern. The lowest radial mode of the m=+1 poloidal mode has the pattern peaked near the plasma periphery. This is the most prominent mode in small-sized, low-density tokamaks. Higher radial modes of any poloidal mode have in general much more favorable power deposition pattern. These modes become propagating in larger, denser tokamak plasmas. The total radial power deposition pattern is obtained from the sum over all modes weighted in accordance with their loading resistances such as those shown in Figs. 6 and 7. Enhancement of the loading resistance by toroidal eigenmode resonances must be taken into consideration in calculations of the weighted sum, since the loading resistance of a lightly damped mode (such as the m=+1) is enhanced strongly by the resonance.

In Table IV the results of computations for four different densities are summarized. At high densities the enhancement factors are close to unity. This shows that the damping strengths at high densities predicted by the present theory tend toward those of Stix's theory for "pure" PFC and DSH damping. At high densities (and also at high ion temperatures) cyclotron damping at the location of the IHB resonance is strong enough to suppress

it unless it is far away from the cyclotron resonance layer (i.e., high proton concentration). This has a significant implication for future ICRF heating of reactor-like plasmas: in spite of the inevitable presence of a few percent impurity protons in deuterium plasmas, the dominant mechanism is essentially pure cyclotron damping. DSH damping, which deposits energy directly in deuterons, should also dominate over PFC damping under reactor-like conditions. For a given amount of Poynting flux, greater power is dissipated at lower densities by both mechanisms. This tendency is particularly strong for the DSH damping. The power dissipated by this mechanism reaches nearly 15 % at the lowest tabulated density. The enhancement factos are 15 and 590 for the PFC and DSH damping for this case. However the latter is likely to be an overestimate because the significant effect of the DSH damping is not included in the E-field calculations and the validity of the theory is questionable.

In Fig. 7(b) the time variation of theoretical loading with enhanced damping is shown. The enhancement factor for the PFC damping is taken to be 15 from Table III, but the factor for the DSH dampng is arbitrarily taken to be 100 rather than 590 as indicated in the table. Although one-to-one correspondence of individual peaks is again impossible to obtain, the general appearance and the level of the loading resistance are much closer to the experimental results (Fig. 3). This shows that the experimentally observed damping strengths are not incompatible

with enhanced cyclotron damping.

The lack of mode structure in the loading curve was interpreted by some researchers as an indication of anomalous power deposition unrelated to fast wave generation. Such "parasitic" loading was thought to be especially severe for antennas without electrostatic shields. However, interpretation of the present experiments is different. At low plasma densities m=+1 mode is the only mode that can carry significant rf power, whereas at higher densities more propagating poloidal modes become available to carry away rf power. Higher radial modes, which may also become propagating, are especially efficient in this respect. Thus, as the density level increases, the level of the loading resistance also rises as seen in Fig. 6. In the highest density case (No. 5) the apparent lack of structure is caused by overlapping of strongly damped modes. When the damping is sufficiently strong, the loading resistance should approach the radiation resistance. The observed loading resistance of 0.8-2 ohms is in good agreement with theoretically predicted radiation resistance. It is recalled that most ATC plasma heating experiments are conducted at these high densities. This indicates that most of the rf power is indeed radiated as the fast wave, and that it is not necessary in the ATC experiments to consider anomalous phenomena to account for the bulk of the power coupled into the tokamak vessel.

In the preceeding paragraphs interpretations of the

experimental results are presented in terms of the enhanced cyclotron damping due to the presence of the two-ion hybrid resonance. A few words of explanation are in order at this point regarding their relation to interpretations based upon mode conversion damping at the two-ion hybrid resonance. The previous analysis is based upon a simple model for the plasma dielectric tensor that results in a second order differential equation. In the limit of the cold plasma approximation the coefficient of the highest order derivative in the equation vanishes at the hybrid resonance, and higher order terms must be retained to describe the wave propagation in the vicinity of the resonance. The analysis in the previous section deals with physical conditions under which thermal effects, primarily PFC and DSH damping, are strong enough such that the second order term remains more important than the higher order terms. Such physical situations would arise when the proton concentration is small, ion temperature is high, or the parallel wavelength is short. Equation (9) expresses a quantitative criterion for the presence of the weak hybrid resonance. The ATC plasmas belong to this category under most plasma heating conditions, and the wave damping data are interpreted in this light * (However, modes near their onset with a long parallel wavelength may not satisfy this criterion and the mode conversion may be important for them.)

*There are theoretical treatments 4,5,23) based upon mode conversion. However, none of them solved boundary value problems to obtan the E-field structure in a bounded plasma, and so were only applicable when the wave absorption was so strong that no waves reflected from the boundaries need be considered. The ATC experimental conditions clearly do not correspond to such cases.

4. Conclusions

The damping length (rather than the cavity-Q factor) of the fast wave propagation in ATC tokamak is measured directly at low plasma densities. The wave damping strength deduced from these measurement is found to be much greater than that predicted by the "pure" PFC and DSH damping theory. Asymmetric location of the region of the strongest damping about the plasma center is also in contrast to the theoretical predictions. The discrepancy in the damping strength is much smaller at higher densities. This implies the predominance of pure cyclotron damping in dense reactor-like deuterium plasmas in spite of the inevitable presence of a few percent impurity protons.

These discrepancies between theory and experiments are attributed to the two-ion hybrid resonance. Unlike interpretations of other experiments based upon linear mode conversion at the hybrid resonance, the current results are explained in terms of enhancement of the cyclotron damping: the hybrid resonance alters the polarization of the wave E-field in such a way as to enhance both the PFC and DSH damping. The enhancement is asymmetric with respect to the plasma center. These explanations are applicable only when the proton concentration is small and the hybrid resonance layer lies close to the cyclotron resonance layer.

Satisfactory performance can be obtained from a simple wave

coupling structure without an electrostatic shield commonly used in the past ICRF heating experiments. The success of the ATC antenna represents a step forward towards a more rugged (presumably all-metal type) structure which could be used in a thermonuclear environment.

The major part of the power coupled into the tokamak vessel is radiated as fast waves and there is no evidence that significant power is lost through so-called "parasitic loading". This is not to say that no rf power is channeled into plasma phenomena other than the fast wave generation. If there are any parasitic effects, they are not of major consequence in dissipating the rf power.

A coupling efficiency (net coupled power/incident power) in excess of 90 % is routinely attained. The total loading resistance is 1-2 ohms under typical plasma heating conditions, and the wave generating efficiency (wave power/net coupled power) of 90-95 % is achieved. The power deposition efficiency (power deposited in plasma/wave power) is about 90 %. The overall efficiency of delivering the power to the plasma is the product of all these efficiencies: approximately 75 % of the generator output power is actually deposited in the plasma. Only that part of the power which is deposited in the central plasma core contributes significantly to plasma heating, and "the heating efficiency 8)" is lower than "the power deposition efficiency" quoted here.

5. Acknowledgement

This work was done while the author was a member of the research staff at the Princeton Plasma Physics Laboratory. The author would like to acknowledge many helpful discussions with Drs. F.W. Perkins and T.H. Stix. He would also like to thank Drs. H. Hsuan, S. Suckewer, T. Nagashima and F.J. Paoloni for providing him bolometric, spectroscopic, charge exchange and rf information. The author is indebted to Messrs. A.J. Sivo and R.S. Christie for construction of the rf equipment and to the ATC operating crew for the machine operation.

References

(1)Takahashi, H., J. de Physique, Coll. C6, Suppl. au n12, Tome 38(1977)171

(2)Adam, J. and Samain, A., Rep. EUR-CEA-FC-579(1971), Assoc. Euratom-CEA, Fontenay-aux-Roses

(3)Stix, T.H., Nucl. Fusion 15(1975)737

(4)Swanson, D.G., Phys. Rev. Lett. 36(1976)316

(5)Perkins, F.W., Nucl. Fusion 17(1977)1197

(6)Takahashi, H., Bull. Am. Phys. Soc., 22(1977)1165

(7)Bol, K., Ellis, R.A.Jr., Eubank, H., Furth, H.P., Jacobsen, R.A., Johnson, L.C., Mazzucato, E., Stodiek, W. and Tolnas, E.L., Phys. Rev. Lett. 29(1972)1495

(8)Takahashi, H., Daughney, C.C., Ellis, R.A.Jr., Goldston, R.J., Hsuan, H., Nagashima, T., Paoloni, F.J., Sivo, A.J. and Suckewer, S., Phys. Rev. Lett. 39(1977)31

(9)Adam, J., Chance, M., Eubank, H., Getty, W., Hinnov, E., Hooke, W., Hosea, J., Jobes, F., Perkins, F., Sinclair, R., Sperling, J. and Takahashi, H., in Proc. of the 5th Conf. on

Plasma Physics and Cont. Nuclear Fusion Res., Tokyo, 1974, (Int. Atomic Energy Agency, Vienna), 1975, Vol.II, p.65

(10)Suckewer, S., Princeton Plasma Phys. Lab., private comm.

(11)Jacquinot, J., McVey, B.D. and Scharer, J.E., Phys. Rev. Lett. 39(1977)88

(12)Takahashi, H., Rep. PPPL-1545(1979), Princeton Plasma Physics Lab.

(13)Bernstein, I.B. and Trehan, S.K., Nucl. Fusion 1(1960)3

(14)Stix, T.H., The Theory of Plasma Waves, McGraw-Hill, New York, 1962, Chapt. 5

(15)Takahashi, H., Bull. Am. Phys. Soc. 20(1975)1241

(16)Paoloni, F.J., Phys. Fluid 18(1975)640

(17)Colestock, P., Princeton Plasma Physics Lab., private comm.

(18)Takahashi, H., Daughney, C.C., Ellis, R.A.Jr., Goldston, R.J., Hsuan, H., Nagashima, T., Paoloni, F.J., Sivo, A.J. and Suckewer, S., Bull. Am. Phys. Soc. 21(1976)1157

(19)Greenough, N., Paoloni, F.J. and Takahashi, H., Bull. Am.

Phys. Soc. 21(1976)1157

(20)TFR Group, 3rd Int. Meet. on Theo. and Exp. Aspects of Heating Toroidal Plasmas, Grenoble, 1976

(21)Studier, P., Hsuan, H., Smith, R.R. and Takahashi, H., Bull. Am. Phys. Soc. 21(1976)1157

(22)Adam, J., Symp. on Plasma Heating and Injection, Varenna, Italy, 1972, C.N.R., Lab. di Fisica del Plasma e di Elettronica Quantistica, Milano, Italy

(23)Jacquinot, J., Paper D4-1, 3rd Topical Conf. on RF Plasma Heating, Pasadena, Calif., 1978

Figure Captions

Fig. 1

Schematic of the wave coupling structure (shown in part).

Fig. 2

Time variation of the wave amplitude (rf envelope) observed by two magnetic probes located 90 degrees around the torus away from the antenna nearly directly above(T) and below(B) the plasma axis.

Fig. 3

Oscillograms of the loading resistance computer outputs. The toroidal magnetic field is different for each oscillogram. The locations of the DSH or PFC resonance surface are indicated.

Fig. 4

(a)Variation of the wave damping length normalized by the toroidal circumference as the toroidal field strength is varied. The abscissa is the major radius location of the DSH or PFC resonance layer. The region of the minimum damping length is asymmetric with respect to the nominal plasma center at 87 cm. (b)Variation of bolometer signal which registers power loss through charge exchange and radiation. The difference between discharges with and without rf pulse is plotted. The nominal extent of the plasma region is indicated. The outer limiter is positioned at 107 cm.

Fig. 5

Oscillogram in the middle shows the perpendicular charge exchange signals at three different energies. Sharp spikes are observed on the two high energy signals coincident with the appearance of a toroidal resonance. The lower oscillogram shows the loading resistance in the expanded time scale. The second peak at 3 ms after the initiation of the rf pulse is coincident with the spikes. The top diagram shows the relative locations of the plasma, antenna and cyclotron resonance layer. The space between the main body plasma and the antenna is filled with a tenuous plasma.

Fig. 6

Oscillograms of the R_S-computer output. The cyclotron resonance surface is located near the plasma center in all cases. Variation of the central electron density for each case is also shown.

Fig. 7

Theoretical loading resistance corresponding to the experimental conditions of the center oscillogram of Fig. 3. (a)Damping strengths based upon minority and second harmonic damping obtained by Stix. (b)Minority damping strength multiplied by an enhancement factor of 15 and the second harmonic damping strength by 100.

Fig. 8

Theoretical loading resistance for the experimental conditions of the top-right oscillogram of Fig. 6. (a)Damping strengths based upon minority and second harmonic damping obtained by Stix. (b)Minority damping strength is multiplied by an enhancement factor of 1.8 and the second harmonic damping strength by 5.2.

Fig. 9

(a)Variation of the E_x-component of the wave electric field across the slab for three different values of the confining B-field : one for which the proton cyclotron resonance falls at the plasma center (0.9 m) and two others for which the resonance is displaced by 0.06 m on either side of the center. The slab half-width is 0.17 m. The hybrid resonance has only small effects on the E_x, but they are asymmetric with respect to the center. (b)Variation of the E_+-field for the same three cases. The hybrid resonance has strong effects on the E_+. Note the appearance of a very steep gradient between the hybrid and cyclotron resonance layers.

Table Captions

Table I

The theoretical wave damping length normalized to the toroidal circumference for the toroidal eigenmodes shown in Fig. 7(a). The normalized damping length is the number of times the waves go around the torus before their amplitudes e-fold. A set of radial(l), poloidal(m) and toroidal(n) eigenmode numbers identifies the resonant mode. The damping lengths are computed based upon "pure" cyclotron damping theories for the proton fundamental cyclotron(I) and deuteron second harmonic(II) damping. The electron Landau/TTMP damping(E) is completely negligible. The wall resistive damping(W) lengths are one-twentieth the values computed for these modes in a cylindrical waveguide made of smooth stainless steel walls. The right-most column(T) lists the total damping lengths.

Table II

The theoretical wave damping length normalized to the toroidal circumference for the toroidal eigenmodes shown in Fig. 8(a). See captions to Table I for symbol explanations. The electron Landau/TTMP damping is completely negligible except where entries are made.

Table III

Influence of the two-ion hybrid resonance on the proton fundamental cyclotron (subscript I) and deuteron second harmonic

(subscript II) damping. Some computed quantities are shown for four different locations of the cyclotron resonance layer (R_c). $n_{||}$ is the parallel refractive index, P the power absorbed in a slab of unit height and depth normalized in such a way that the Poynting flux is 1 MW per unit height of the slab, J_I and $J_{II}/(k_A a)^2$ the enhancement factors, Q the quality factor, and L_D/L the damping length normalized by the toroidal circumference.

Table IV

Influence of the two-ion hybrid resonance on the proton fundamental cyclotron and deuteron second harmonic damping. Some computed quantities are shown for four different values of the on-axis plasma density (n_{e0}). See captions to Table III for symbol explanations.

Table I

(l, m, n)	I	II	E	W	T
(1, 1, 3)	170	230	-	13	12
(1, 1, 4)	56	100	-	11	9
(1, 2, 3)	240	410	-	17	16
(1, 2, 4)	79	150	-	13	11
(1, 3, 4)	95	220	-	17	14

Table II

(l, m, n)	I	II	E	W	T
(1,-1, 1)	76	1.7	-	55	1.6
(1,-1, 2)	29	2.4	-	27	2.0
(1, 0, 6)	5.0	5.4	160	9.2	2.0
(1, 1,10)	3.1	24	80	17	2.3
(2, 1, 1)	81	1.7	-	54	1.7
(2, 1, 2)	33	2.7	-	23	2.3
(1, 2, 8)	6.5	20	140	8.6	3.1
(1, 3, 8)	7	20	160	9.6	3.3

Table III

R_c	m	0.98	0.94	0.90	0.86
n_{II}		28	29	30	31
P_I	kW/m^2	25	78	55	6.0
P_{II}	kW/m^2	1.6	4.0	2.0	0.11
J_I		7.2	2.8	1.8	1.2
$J_{II}/(k_A a)^2$		64	13	5.2	2.1
Q_I		560	180	230	2100
Q_{II}		8500	3400	6500	120000
$(L_D/L)_I$		14	4.5	6.4	58
$(L_D/L)_{II}$		220	89	180	3100

Table IV

n_{e0}	$10^{19}/m^3$	0.8	1.5	2.5	3.5
$n_{\parallel}$		14	22	30	36
P_I	kW/m^2	300	95	55	40
P_{II}	kW/m^2	44	12	2.0	0.55
J_I		15	3.1	1.8	1.3
$J_{II}/(k_A a)^2$		590	54	5.2	1.1
Q_I		570	150	230	360
Q_{II}		3900	1200	6500	26000
$(L_D/L)_I$		1.2	3.7	6.4	8.8
$(L_D/L)_{II}$		7.1	30	180	640

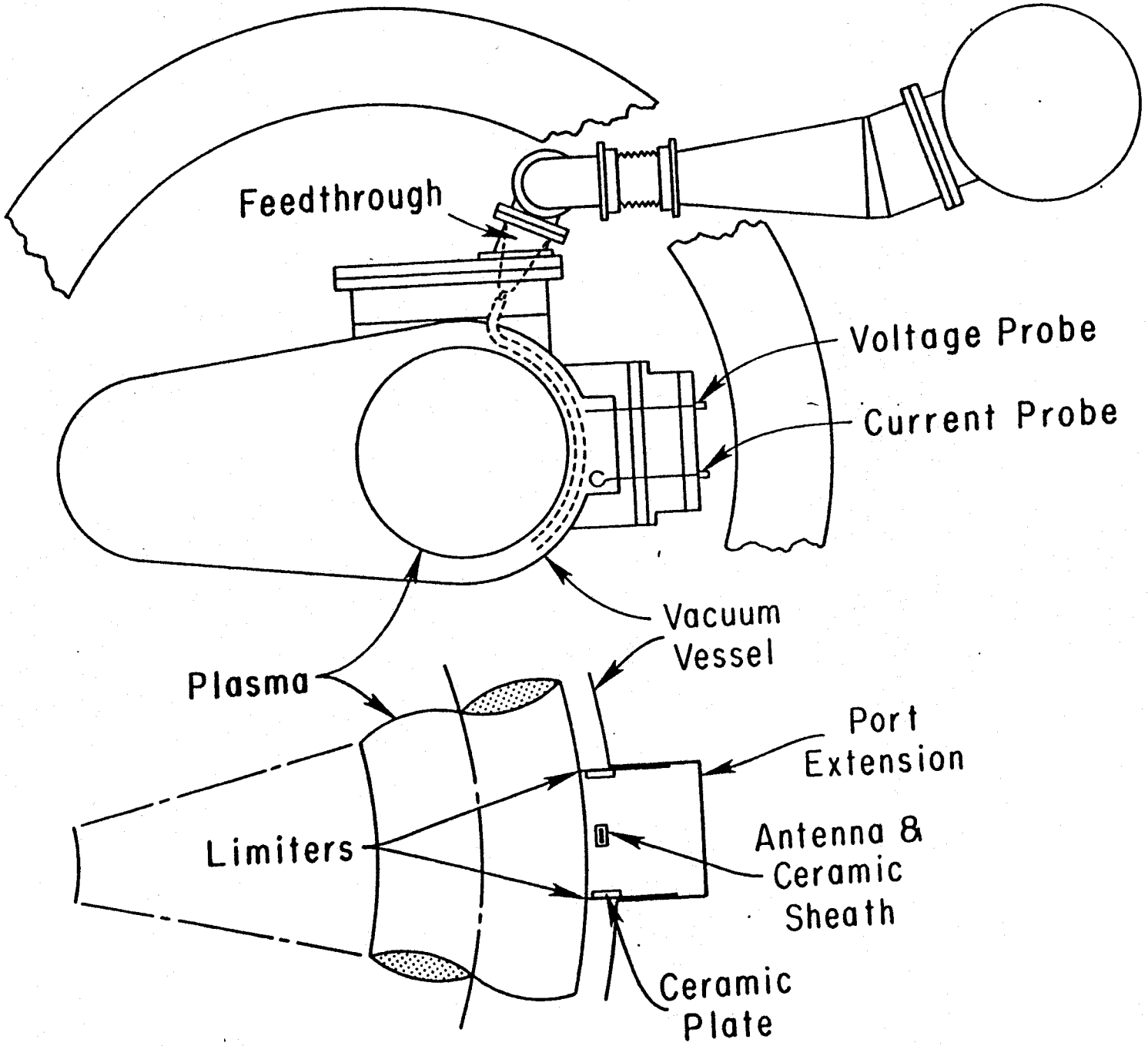
Feedthrough
Voltage Probe
Current Probe
Vacuum
Vessel
Plasma
Port
Extension
Limiters
Antenna &
Ceramic
Sheath
Ceramic
Plate

Fig. 1

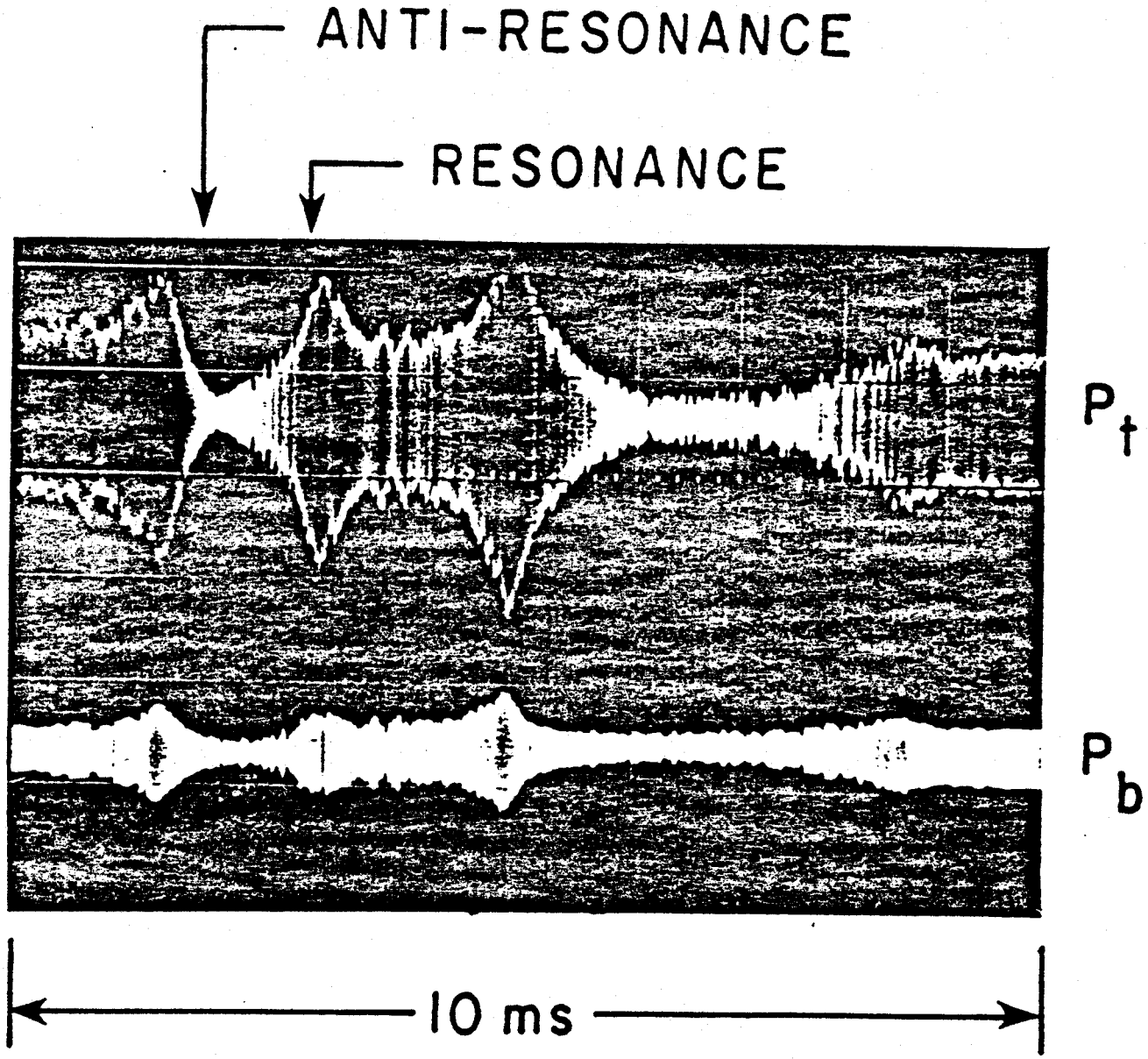

Fig. 2

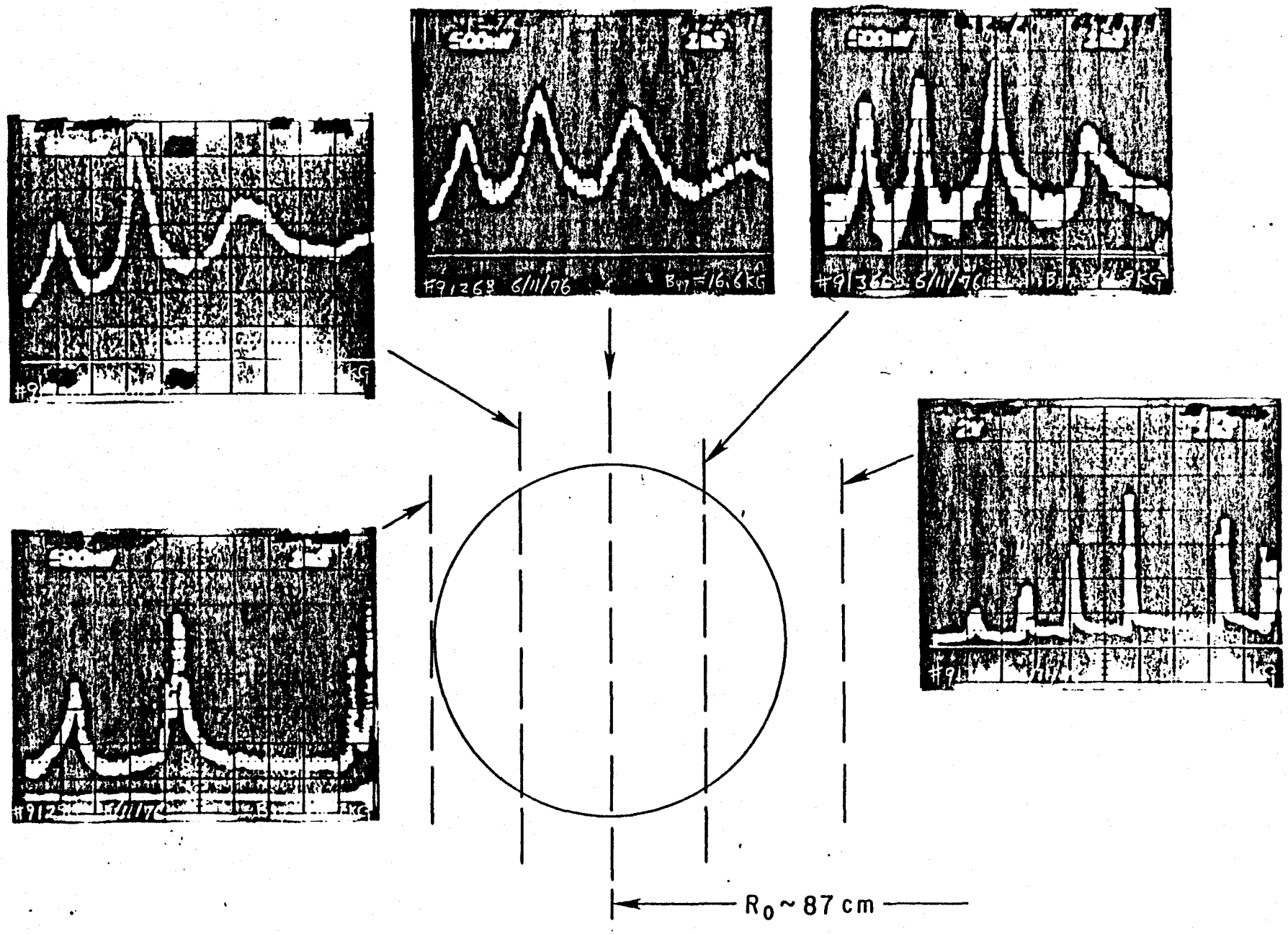

Fig. 3

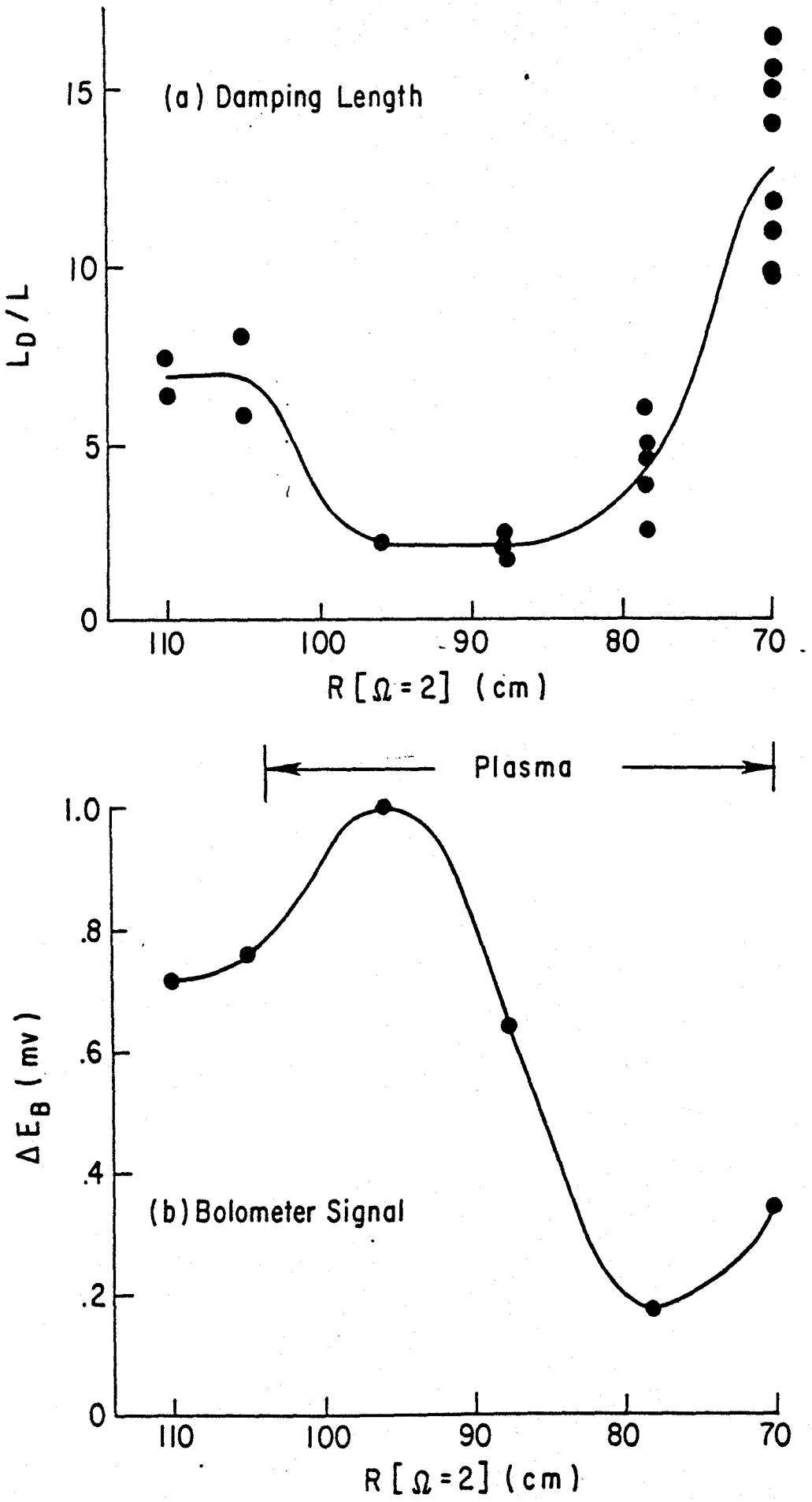
(a) Damping Length
L_D/L
15
10
5
0
110
100
90
80
70
R [Ω = 2] (cm)
Plasma
(b) Bolometer Signal
ΔE_B (mv)
1.0
.8
.6
.4
.2
0
110
100
90
80
70
R [Ω = 2] (cm)

Fig. 4

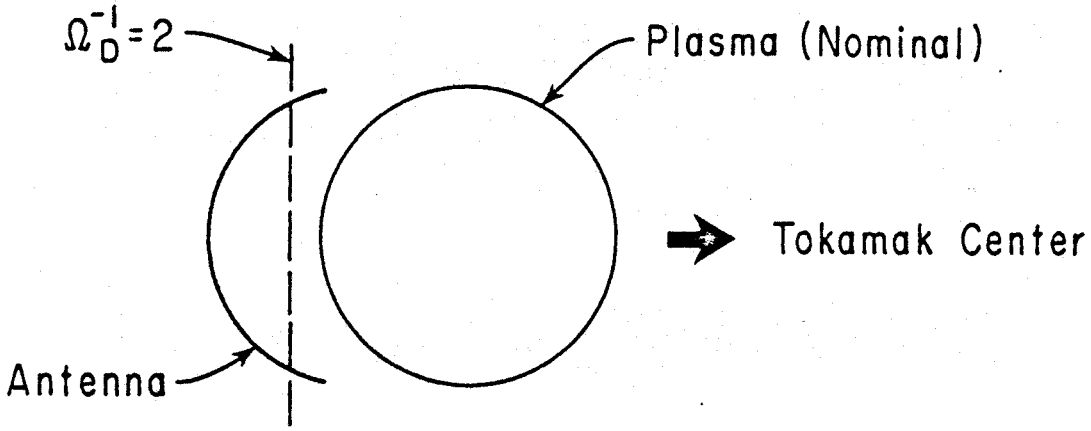
$\Omega_D^{-1} = 2$
Plasma (Nominal)
Tokamak Center
Antenna

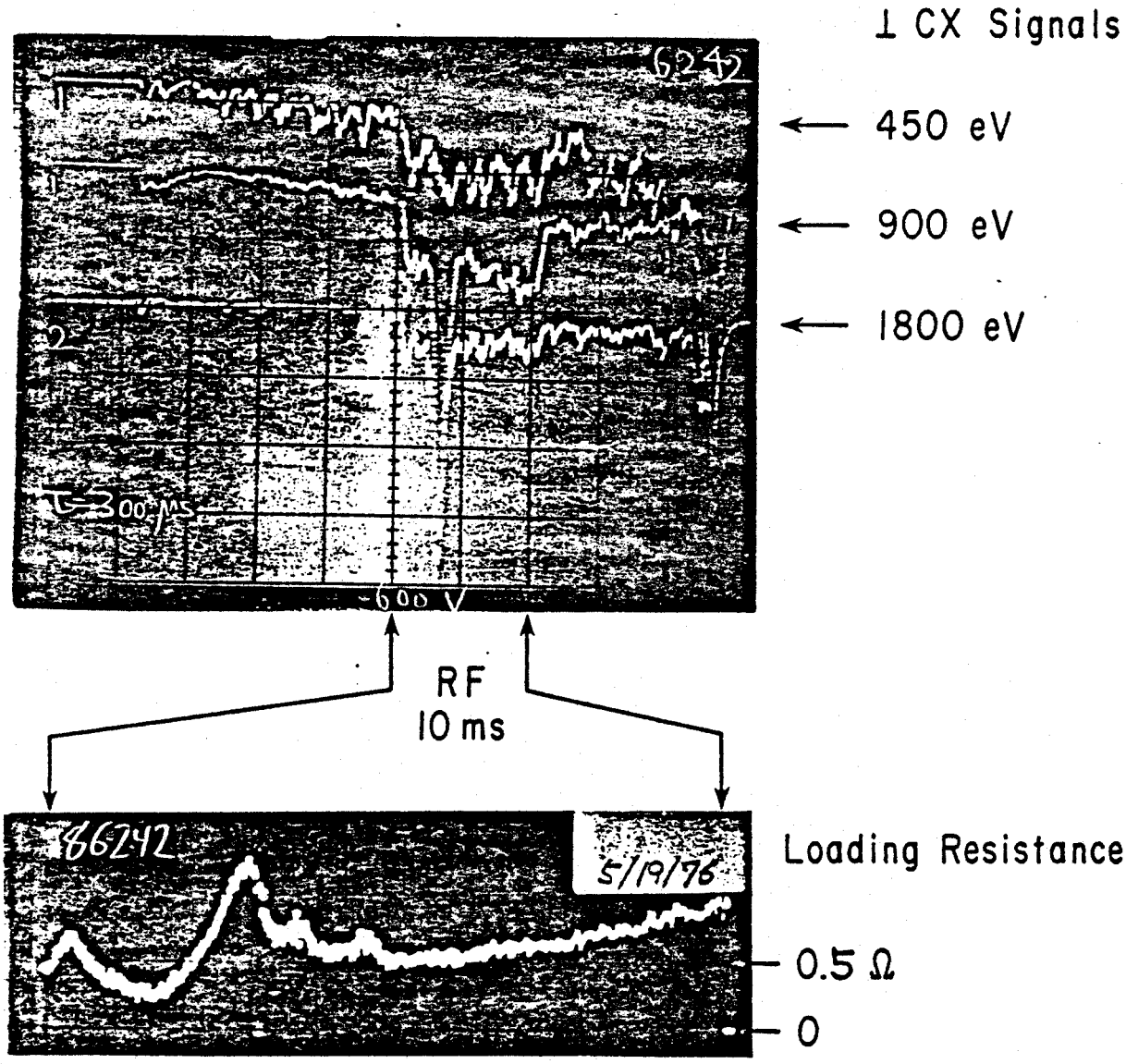
⊥ CX Signals
66242
450 eV
900 eV
1800 eV
RF
10 ms
66242
5/19/76
Loading Resistance
0.5 Ω
0

Fig. 5

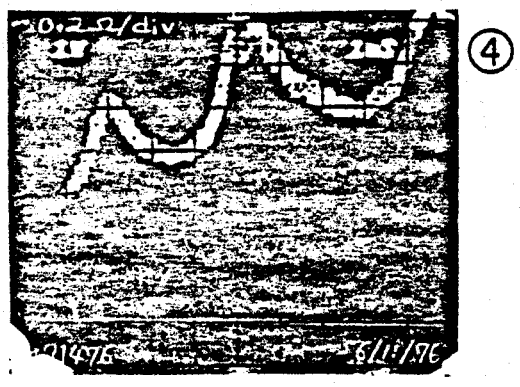
0.2Ω/div
1mS
6/11/76

④

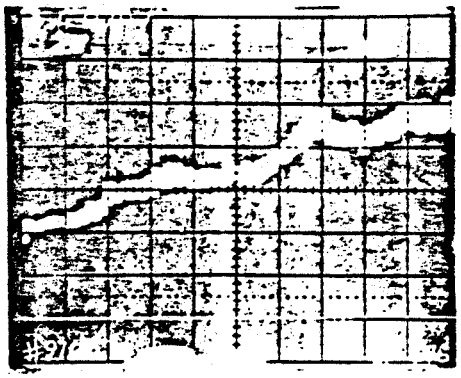

⑤


0.5Ω/div
1mS
6/11/76

③

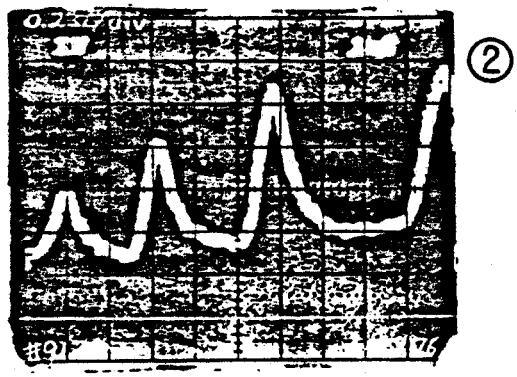
0.2Ω/div
1mS
#91
76

②

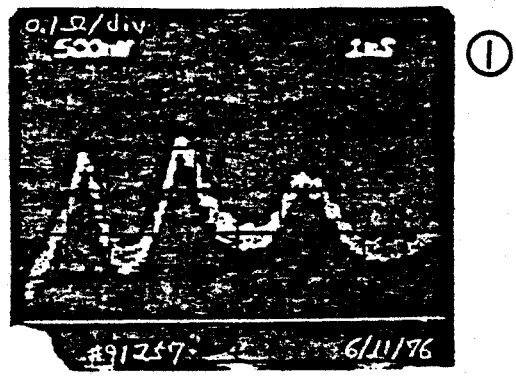
0.1Ω/div
500W
1mS
#91257
6/11/76

①

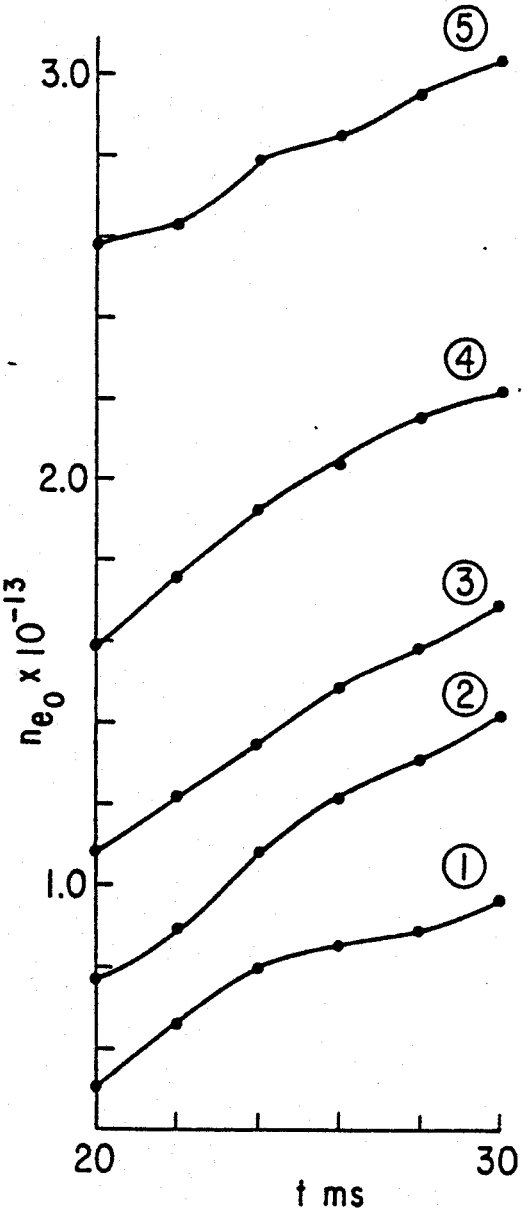
⑤
3.0
④
2.0
③
②
①
1.0
$n_{e_0} \times 10^{-13}$
20
30
t ms

Fig. 6

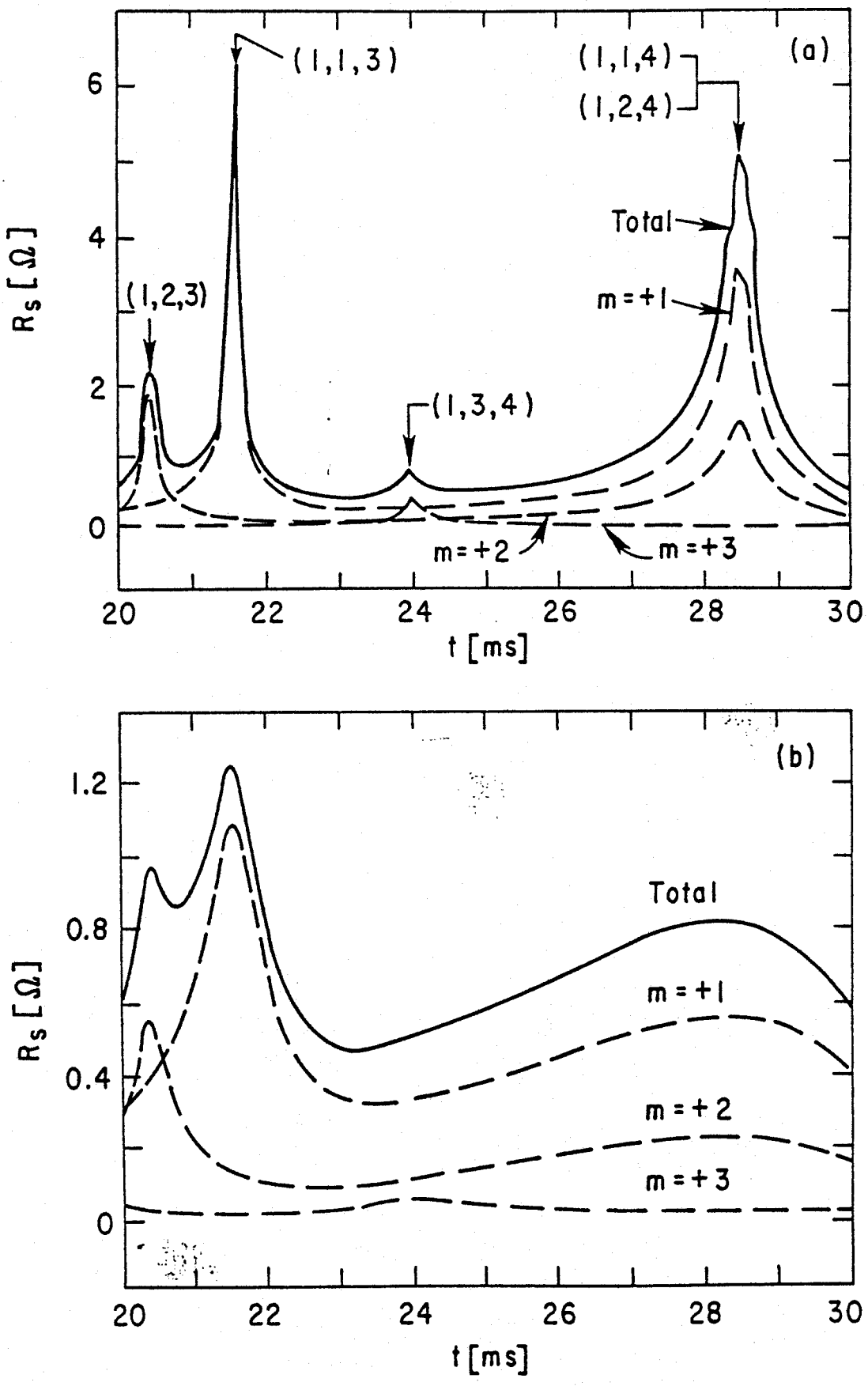
(a)
(1,1,3)
(1,1,4)
(1,2,4)
Total
(1,2,3)
m=+1
(1,3,4)
m=+2
m=+3
R_s [Ω]
t [ms]
(b)
Total
m=+1
m=+2
m=+3
R_s [Ω]
t [ms]

Fig. 7

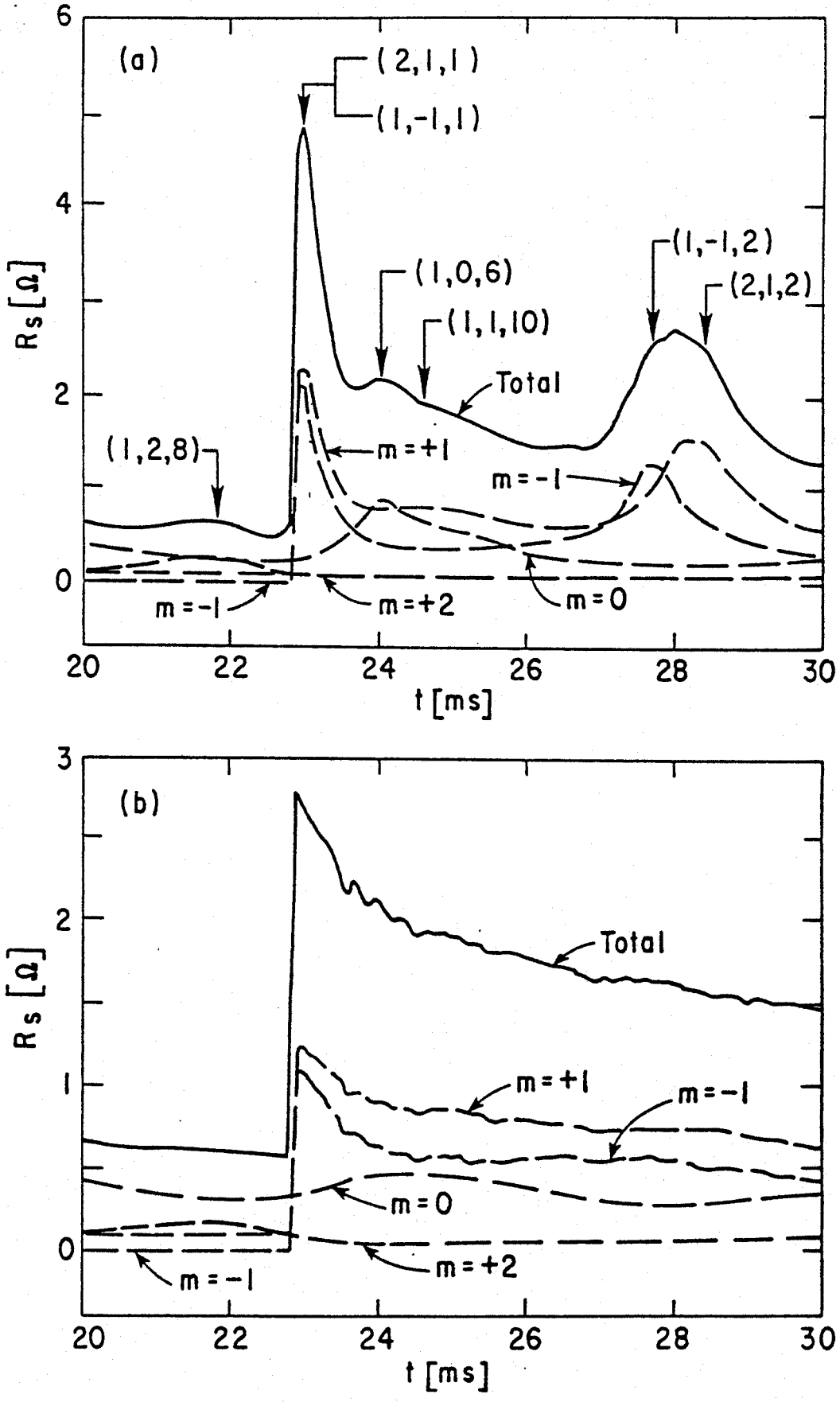
(a)
(2,1,1)
(1,-1,1)
(1,-1,2)
(2,1,2)
(1,0,6)
(1,1,10)
Total
(1,2,8)
m=+1
m=-1
m=-1
m=+2
m=0
R_s [Ω]
t [ms]
(b)
Total
m=+1
m=-1
m=0
m=-1
m=+2
R_s [Ω]
t [ms]

Fig. 8

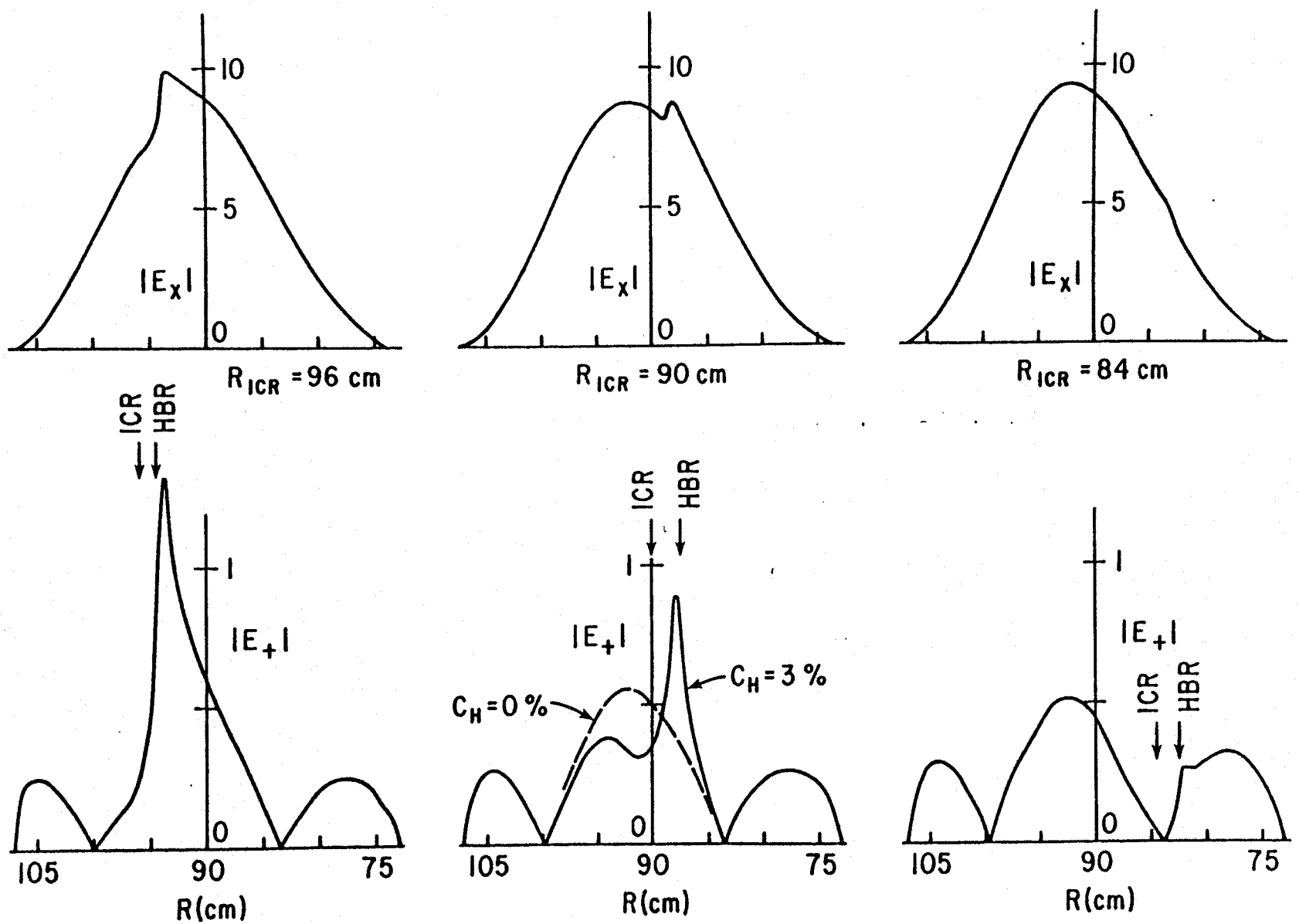
10
5
0
$|E_x|$
R_{ICR} = 96 cm
R_{ICR} = 90 cm
R_{ICR} = 84 cm
ICR
HBR
1
$|E_+|$
C_H = 0 %
C_H = 3 %
105
90
75
R(cm)

Fig. 9